JOURNAL OF GEOPHYSICAL RESEARCH, VOL. 89, NO. B12, PAGES 10,087–10,101, NOVEMBER 10, 1984

Mechanics of Fold-and-Thrust Belts and Accretionary Wedges: Cohesive Coulomb Theory

F. A. DAHLEN AND JOHN SUPPE

Department of Geological and Geophysical Sciences, Princeton University, New Jersey

DAN DAVIS[1]

Department of Earth, Atmospheric, and Planetary Sciences, Massachusetts Institute of Technology, Cambridge

A critically tapered fold-and-thrust belt or submarine accretionary wedge is one that is on the verge of Coulomb failure everywhere, including its base where frictional sliding along a decollement is assumed to be occurring. Cohesion within a wedge can add significantly to the overall strength near the toe; the effect of this is to decrease the near-toe taper, leading to a critical topographic profile that is concave upward if the decollement is planar. We obtain an approximate self-consistent solution for the state of stress within a thin-skinned cohesive critical Coulomb wedge, and determine the relationship between the wedge taper and its strength and basal friction. The theory is then applied to the presently deforming fold-and-thrust belt of western Taiwan. Fitting of theoretical critical wedge shapes to topographic profiles and measurements of the step-up angles of thrust faults from the basal decollement are used to constrain the Taiwan wedge strength parameters. An attractive assertion fully consistent with all the observations is that the mechanics of fold-and-thrust belts and accretionary wedges is governed by normal frictional and fracture strengths of rocks measured in the laboratory. In particular, if Byerlee's law $\mu_b = 0.85$ is adopted as the coefficient of sliding friction on the base, we find a coefficient of internal friction $\mu = 0.9$–1.0 in the wedge and a wedge cohesion $S_0 = 5$–20 MPa. Other solutions having strengths and ambient stresses up to 4 times lower than this can also, however, satisfy the data.

INTRODUCTION

This paper is a continuation of an earlier one (*Davis et al.* [1983], hereafter referred to as Wedge 1) in which we presented a theoretical model for the gross mechanics of fold-and-thrust belts and accretionary wedges along compressive plate boundaries. In that paper we considered these wedge-shaped zones of deformation to be analogous to the wedges of soil or snow that form in front of moving bulldozers. When an initially thin layer of Coulomb material is encountered by a bulldozer or plate boundary, it deforms, steepening its surface slope, until a critical taper is attained that allows stable sliding to occur along the base without continued internal deformation. If additional material is encountered and accreted at the toe, the wedge will grow self-similarly, maintaining its critical taper.

The theoretical treatment of this problem in Wedge 1, which yielded a formula relating the wedge taper to its material properties, was purposely simplified in order to focus attention on the essential physical concepts and geological observations. In the present paper we present a more systematic analysis, determining the state of stress everywhere within a critical wedge by solving the static equilibrium equations subject to the appropriate boundary conditions. Furthermore we consider the influence of an additional material parameter, wedge cohesion, which gives rise to a concave curvature of the critical topographic surface and affects the orientation of the principal stresses and Coulomb fractures within the wedge. After confirming that the more complete theory accurately describes the results of the laboratory sandbox experiment described in Wedge 1, we apply it to the active fold-and-thrust belt of western Taiwan. Taking into account the extensive structural and fluid-pressure data available there, we analyze the shape of the topographic surface and the angles at which thrust faults step up from the basal decollement. Our principal conclusion that the gross geometry and structure of the Taiwan wedge are consistent with normal laboratory frictional and fracture strengths of sedimentary rocks is unchanged; in fact it is reinforced.

In the interest of brevity we have not attempted to make this paper self-contained; some familiarity with the contents of Wedge 1 is presumed. In particular that earlier paper contains the geological justification for both the use of a bulldozer-wedge model and the choice of a Coulomb material behavior, as well as a discussion of the expected realm of applicability of the theory within the earth. A few minor changes in notation have been made, partly as a result of a change from the system of Cartesian coordinates employed earlier. In addition we have adopted the convention prevalent in continuum mechanics that a tensile stress is positive, and we now denote effective stresses by an overbar rather than an asterisk.

CRITICAL COULOMB WEDGE THEORY

The natural coordinate system for examining the state of stress within a wedge-shaped region is a system of cylindrical coordinates with the origin at the toe. Such a system was adopted by *Chapple* [1978] in his analysis of a perfectly plastic wedge having a constant yield stress. We shall use r to denote the radial distance from the origin and θ to denote the angular depth, measured down from the upper surface (see Figure 1). The location of the origin must be allowed to vary along the basal decollement, which is assumed to be planar, because of the topographic curvature exhibited by a critical cohesive wedge. This inconvenience, which is dictated by our use of cylindrical coordinates, is more than offset by the ease

[1] Now at Lamont-Doherty Geological Observatory of Columbia University, Palisades, New York.

Paper number 4B0413.
0148-0227/84/004B-0413$05.00

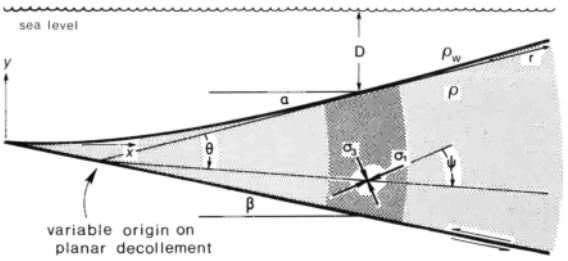

Fig. 1. Schematic cross section of a critical cohesive Coulomb wedge, illustrating some of the geometrical quantities arising in the analysis. Heavy shading denotes region of wedge for which the cylindrical coordinates r, θ shown are appropriate.

with which boundary conditions along the top and bottom of the wedge can be stipulated and satisfied. The slopes of the upper surface and decollement will again be denoted by α and β, respectively, and we shall now use ψ to denote the angle of inclination between the axis of greatest principal compressive stress and a radius vector, as shown.

A critical wedge, by definition, is one on the verge of shear failure everywhere. Using our new sign convention, the empirical Coulomb criterion relating the shear and normal tractions across a plane at failure is

$$|\tau| = S_0 - \mu\bar{\sigma}_n \tag{1}$$

where S_0 is the cohesion and $\mu = \tan\phi$ is the coefficient of internal friction. The effective stress $\bar{\sigma}_n$ appearing in (1) is given by

$$\bar{\sigma}_n = \sigma_n + p_f \tag{2}$$

where p_f is the pore-fluid pressure. Alternatively, if expressed in terms of the effective principal stresses $\bar{\sigma}_1$ and $\bar{\sigma}_3$, the failure criterion (1) takes the form

$$\bar{\sigma}_1 = \left(\frac{1+\sin\phi}{1-\sin\phi}\right)\bar{\sigma}_3 - C_0 \tag{3}$$

where

$$C_0 = 2S_0\left(\frac{1+\sin\phi}{1-\sin\phi}\right)^{1/2} \tag{4}$$

is the uniaxial compressive strength [*Jaeger and Cook*, 1969].

It is straightforward to show that the state of two-dimensional stress within a cylindrical wedge at failure is given by

$$\tfrac{1}{2}(\sigma_\theta - \sigma_r) = \frac{S_0\cot\phi - \bar{\sigma}_\theta}{\csc\phi\sec 2\psi - 1} \tag{5a}$$

$$\tau_{r\theta} = \frac{\tan 2\psi(S_0\cot\phi - \bar{\sigma}_\theta)}{\csc\phi\sec 2\psi - 1} \tag{5b}$$

These constitutive relations provide a complete description of the deviatoric stresses $\frac{1}{2}(\sigma_\theta - \sigma_r)$ and $\tau_{r\theta}$ in terms of two unknowns, the effective stress $\bar{\sigma}_\theta$ and the stress orientation angle ψ. Analysis of the Mohr circle geometry depicted in Figure 2 is one method of deriving (5). The equations of static equilibrium, which must be satisfied throughout the wedge, are

$$r\frac{\partial\sigma_r}{\partial r} + \frac{\partial\tau_{r\theta}}{\partial\theta} + \sigma_r - \sigma_\theta + \rho g r\sin(\theta-\alpha) = 0 \tag{6a}$$

$$r\frac{\partial\tau_{r\theta}}{\partial r} + \frac{\partial\sigma_\theta}{\partial\theta} + 2\tau_{r\theta} + \rho g r\cos(\theta-\alpha) = 0 \tag{6b}$$

where ρ is the wedge density and g is the acceleration of gravity. The upper surface of a subaerial wedge must be traction free. More generally, for a submarine wedge overlain by water of density ρ_w and local depth D, the upper boundary conditions are

$$\tau_{r\theta} = 0 \qquad \sigma_\theta = -p_f = -\rho_w g D \tag{7}$$

on $\theta = 0$. The shear traction resisting frictional sliding on the base is assumed to be

$$\tau_{r\theta} = -\mu_b\bar{\sigma}_\theta \tag{8}$$

on $\theta = \alpha + \beta$, where $\mu_b = \tan\phi_b$ is the basal coefficient of friction. This empirical friction law is the basal counterpart of the Coulomb failure criterion (1) within the wedge.

Equations (5)–(8) constitute a well-posed hyperbolic boundary value problem for the stresses σ_r, σ_θ, and $\tau_{r\theta}$. The effective principal stresses are given in terms of σ_r, σ_θ, and $\tau_{r\theta}$ by

$$\bar{\sigma}_1 = \bar{\sigma}_\theta - \tfrac{1}{2}(\sigma_\theta - \sigma_r) - \left[\tfrac{1}{4}(\sigma_\theta - \sigma_r)^2 + \tau_{r\theta}{}^2\right]^{1/2} \tag{9a}$$

$$\bar{\sigma}_3 = \bar{\sigma}_\theta - \tfrac{1}{2}(\sigma_\theta - \sigma_r) + \left[\tfrac{1}{4}(\sigma_\theta - \sigma_r)^2 + \tau_{r\theta}{}^2\right]^{1/2} \tag{9b}$$

or alternatively, by

$$\bar{\sigma}_1 = \bar{\sigma}_\theta - \tfrac{1}{2}(\sigma_\theta - \sigma_r)(1 + \sec 2\psi) \tag{10a}$$

$$\bar{\sigma}_3 = \bar{\sigma}_\theta - \tfrac{1}{2}(\sigma_\theta - \sigma_r)(1 - \sec 2\psi) \tag{10b}$$

A common method of solving for the stress in problems such as this is to integrate the characteristic equations defining the slip lines along which failure can occur [*Hill*, 1950]. In the present instance this must be done numerically on a two-dimensional grid; such an approach has recently been adopted in the perfectly plastic case by *Stockmal* [1983]. We shall present here a much simpler approximate solution which should be valid in all wedges of geological interest. A major advantage of this solution is that its dependence on the various geometrical and material parameters is fairly explicit, allowing a wide range of different possible models to be easily and systematically explored. As in Wedge 1, we shall develop the theory for a submarine wedge, knowing we can always find the corresponding result for a subaerial fold-and-thrust belt by setting $\rho_w = 0$.

The Critical-Taper Equation

The principal approximation we shall make is that

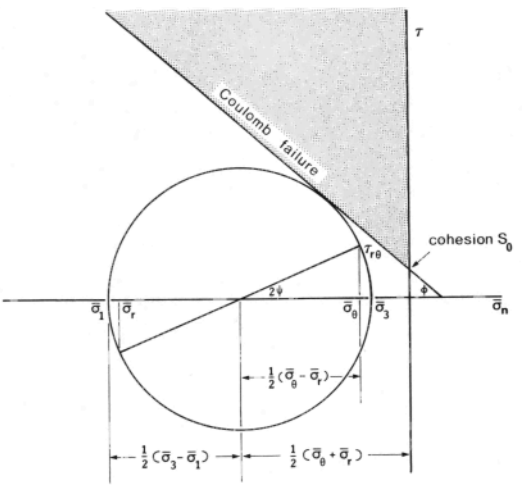

Fig. 2. Mohr diagram illustrating the state of two-dimensional effective stress at an arbitrary point within the wedge.

$$\alpha + \beta \ll 1 \tag{11}$$

The thin-skinned nature of actual wedges justifies this small-angle or narrow-taper approximation. We shall also restrict consideration to regions sufficiently far from the vertex, by requiring that

$$\rho g r / S_0 \gg 1 \tag{12}$$

In practice, this latter restriction is seldom significant, as we shall see. Upon employing (11) and (12) in the integration of (6*b*), we find to lowest order that

$$\bar{\sigma}_\theta = -(1 - \lambda)\rho g r \theta \tag{13}$$

where

$$\lambda = \frac{p_f - \rho_w g D}{\rho g r \theta} \tag{14}$$

is the *Hubbert and Rubey* [1959] fluid-pressure ratio, suitably generalized to the submarine case as in Wedge 1. Equations (13) and (14) simply state that the "vertical" stress in a thin-skinned wedge is approximately lithostatic, which accords well with intuition.

Integration of (6*a*) making use of (5*a*) and (13) in addition to (11) and (12) now leads to an alternative first-order formula for the shear stress, namely,

$$\tau_{r\theta} = (\rho - \rho_w) g r \alpha \theta + 4(1 - \lambda)\rho g r \int_0^\theta \frac{\theta \, d\theta}{\csc \phi \sec 2\psi - 1} + 2 S_0 \cot \phi \int_0^\theta \frac{d\theta}{\csc \phi \sec 2\psi - 1} \tag{15}$$

Equations (5*b*) and (15) together yield the formula

$$(1 - \rho_w/\rho)\alpha\theta + 4(1 - \lambda) \int_0^\theta \frac{\theta \, d\theta}{\csc \phi \sec 2\psi - 1} + 2\left(\frac{S_0}{\rho g r}\right) \cot \phi \int_0^\theta \frac{d\theta}{\csc \phi \sec 2\psi - 1} = \frac{\tan 2\psi}{\csc \phi \sec 2\psi - 1} \left[(1 - \lambda)\theta + \left(\frac{S_0}{\rho g r}\right) \cot \phi \right] \tag{16}$$

which allows the angle ψ to be determined everywhere by a straightforward one-dimensional numerical quadrature, starting from $\psi = 0$ at $\theta = 0$. For a given α, (16) is integrated downward until the condition (8) for frictional sliding along the base of the wedge is satisfied, thus determining β. For a given β, iteration of (16) is required to find the surface slope α that allows the basal boundary condition to be satisfied. In either case, the wedge taper $\alpha + \beta$ is given by

$$\alpha + \beta = \frac{(1 - \rho_w/\rho)\beta + (1 - \lambda_b)\mu_b - Q(S_0/\rho g r) \cot \phi}{(1 - \rho_w/\rho) + (1 - \lambda)K} \tag{17}$$

where λ_b is the basal value of the fluid-pressure ratio and

$$K = 4(\alpha + \beta)^{-2} \int_0^{\alpha+\beta} \frac{\theta \, d\theta}{\csc \phi \sec 2\psi - 1} \tag{18a}$$

$$Q = 2(\alpha + \beta)^{-1} \int_0^{\alpha+\beta} \frac{d\theta}{\csc \phi \sec 2\psi - 1} \tag{18b}$$

Equation (17), which we call the critical-taper equation, follows directly from comparing (8) and (15) on the base $\theta = \alpha + \beta$. The condition that the wedge be in a state of horizontal compression rather than extension is that $0 \le \psi \le \pi/4$, implying that the coefficients K and Q are bounded by

$$0 \le K, Q \le \frac{2}{\csc \phi - 1} \tag{19}$$

In the above derivation, it has been tacitly assumed that the density ρ and the various strength parameters S_0, μ, λ, μ_b, and λ_b are all constants. It is obvious that the analysis could be readily extended to deal with spatially variable parameters, but this does not seem warranted at the present time given the quality of available geological data. For a given constant decollement dip β and strength parameters μ, λ, μ_b, and λ_b the critical-taper equation (17) gives the variable surface slope α as a function of the dimensionless radial distance $\rho g r / S_0$ from the origin.

The basal decollement of a critically tapered wedge must be weaker than the material composing the wedge in order for stable sliding to occur along the base. Letting $H = r(\alpha + \beta)$ denote the local wedge thickness, we can write this wedge existence condition as

$$\mu_b(1 - \lambda_b) \le \mu(1 - \lambda) + S_0/\rho g H \tag{20}$$

Far from the toe, in the limit $\rho g r / S_0 \to \infty$, the critical taper approaches a constant asymptotic value

$$\alpha + \beta \to \frac{(1 - \rho_w/\rho)\beta + (1 - \lambda_b)\mu_b}{(1 - \rho_w/\rho) + (1 - \lambda)K} \tag{21}$$

that is independent of the cohesion S_0. This limiting taper, corresponding to negligible cohesion, agrees in form with that derived in Wedge 1 where cohesion was ignored. The integral (18*a*) defining K in (21) differs slightly from that obtained previously, partly because both solutions are approximate and partly because the new definition of ψ in cylindrical coordinates is different. The existence condition for a large wedge is the same as that for a noncohesive wedge, namely, $(1 - \lambda_b)\mu_b \le (1 - \lambda)\mu$ or $\phi_b' \le \phi$, where

$$\phi_b' = \arctan [\mu_b(1 - \lambda_b)/(1 - \lambda)] \tag{22}$$

is an adjusted basal friction angle allowing for a possible difference between λ_b and λ. Moving toward the toe from the back, the taper $\alpha + \beta$ is seen from (17) and (19) to decrease from its noncohesive asymptote (21), where it is maximum. The curvature of the critical surface topography is as a result concave upward for a wedge of uniform properties, as indicated earlier.

The effective state of stress along the upper surface $\theta = 0$ is given by $\bar{\sigma}_\theta = \bar{\sigma}_3 = 0$ and $\bar{\sigma}_r = \bar{\sigma}_1 = -C_0$, where C_0 is the uniaxial compressive strength defined by (4). The variation of

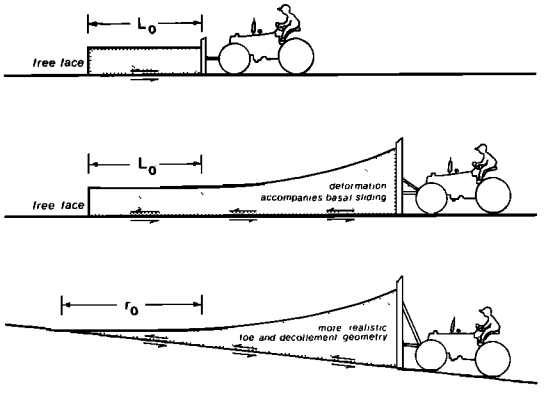

Fig. 3. Cartoon comparing the present analysis with that of *Hubbert and Rubey* [1959].

ψ in the region just below the upper surface can be shown by expansion of (16) to be

$$\psi \approx \left[1 + \frac{(1 - \rho_w/\rho)\alpha(\csc\phi - 1)}{2(S_0/\rho g r)\cot\phi + 2(1 - \lambda)\theta}\right]\theta \tag{23}$$

near $\theta = 0$. The noninterchangeability of the limits $\theta \to 0$ and $S_0 \to 0$ in (23) is associated with the existence of an upper boundary layer in which cohesion plays a dominant role even near the back of the wedge. A finite amount of cohesion, no matter how slight, is required to insure that $\bar{\sigma}_1$ is aligned with the surface topography so that $\psi \to 0$ as $\theta \to 0$. The finite surface inclination ψ_0 of $\bar{\sigma}_1$ at the top of a strictly noncohesive wedge is given by

$$\psi_0 = \lim_{\theta \to 0} \lim_{S_0 \to 0} \psi = \frac{(1 - \rho_w/\rho)\alpha(\csc\phi - 1)}{2(1 - \lambda)} \tag{24}$$

The thickness of the upper boundary layer in a cohesive wedge is seen from (23) to be of order $h = S_0/[\mu(1 - \lambda)\rho g]$. In the region near the toe where $H \lesssim h$ the entire wedge is dominated by cohesion. The concave topography associated with the near-toe reduction in taper is a direct consequence of the increasing importance of cohesion relative to the overall wedge strength as H decreases.

According to (17), the critical surface slope α is negative for distances r from the toe less than

$$r_0 = \frac{QS_0\cot\phi}{\rho g[(1 - \lambda_b)\mu_b + (1 - \lambda)K\beta]} \tag{25}$$

Equation (25) gives the maximum length of a wedge-shaped body with zero surface slope that can be thrust over a dipping basel decollement without undergoing internal Coulomb failure. It is reminiscent of a well-known formula derived by *Hubbert and Rubey* [1959] for the maximum length L_0 of a rectangular thrust sheet overlying a horizontal decollement. By implication, an initially rectangular body longer than L_0 will deform until it attains a critical taper toward its rear (see Figure 3). The theory presented here calculates this critical taper explicitly, allowing for a dipping decollement and avoiding the artificial leading free face of Hubbert and Rubey.

To construct theoretical wedge profiles, we must contend, as mentioned, with the variable position of the origin along the decollement. Let x and y be a system of Cartesian coordinates with a fixed origin and y pointing upward, so that the linear equation $y + x\tan\beta = 0$ defines the position of the decollement as shown in Figure 1. In the small-angle approximation, the curve describing the concave upper surface of a critically tapered wedge can be written in parameterized form in these coordinates as

$$x(r) = r + \int_{r_0}^{r} (\alpha + \beta)^{-1} r\alpha'\, dr \tag{26a}$$

$$y(r) = \int_{r_0}^{r} \alpha\, dr + \int_{r_0}^{r} \alpha(\alpha + \beta)^{-1} r\alpha'\, dr \tag{26b}$$

where the terms depending on $\alpha' = d\alpha/dr$ account for the movement of the origin. In setting the lower limit of integration in (26) equal to r_0, we are stipulating that the front of the wedge consists of a flat-topped, triangular undeformed Hubbert-Rubey toe.

Step-Up of Thrusts From the Basal Decollement

At every point in a critically tapered wedge, there will be two planes oriented at angles $\pm(\pi/4 - \phi/2)$ with respect to the $\bar{\sigma}_1$ axis on which the failure criterion will be satisfied [*Jaeger and Cook*, 1969]. Knowing this, it is a simple matter to reconstruct the slip lines within the wedge once the orientation ψ of $\bar{\sigma}_1$ has been determined everywhere. Forward verging slip lines dip at an angle

$$\delta = \frac{\pi}{4} - \frac{\phi}{2} - \psi \tag{27}$$

relative to the local radius vector at any point, whereas backward verging ones dip at the steeper angle

$$\delta + 2\psi = \frac{\pi}{4} - \frac{\phi}{2} + \psi \tag{28}$$

It is particularly simple to determine ψ_b and thus $\delta_b = \pi/4 - \phi/2 - \psi_b$ on the base of the wedge; we only need to compare (5*b*) with the boundary condition (8), making use of (13). This leads to the relation

$$[\mu(1 - \lambda) + S_0/\rho g H]\sin 2\psi_b = \mu_b(1 - \lambda_b)[(1 + \mu^2)^{1/2} - \mu\cos 2\psi_b] \tag{29}$$

where, as before, $H = r(\alpha + \beta)$ is the local wedge thickness. Equation (29), which serves to define ψ_b implicitly, can be rewritten in terms of ϕ and ϕ_b' as

$$\sin(\phi_b' + 2\psi_b) = \frac{\sin\phi_b'[1 + (S_0/\rho g\bar{H})\cos\phi\cos 2\psi_b]}{\sin\phi + (S_0/\rho g\bar{H})\cos\phi} \tag{30}$$

where we have defined the effective wedge thickness

$$\bar{H} = (1 - \lambda)H \tag{31}$$

An alternative direct derivation of this latter form can be based on the Mohr circle geometry shown in Figure 4. In the limit of negligible cohesion, both (29) and (30) approach the result given in Wedge 1, namely,

$$\psi_b \to \frac{1}{2}\arcsin\left(\frac{\sin\phi_b'}{\sin\phi}\right) - \frac{\phi_b'}{2} \tag{32}$$

We shall make use of these results below in interpreting the observed basal step-up angle δ_b of forward verging thrust faults in western Taiwan. The underlying assumption, which seems quite reasonable, is that the observed faults were formed as fresh fractures coinciding with the slip lines in a Coulomb material. In the special case of a wedge and decollement of identical properties, i.e., $S_0 = 0$ and $\phi_b' = \phi$, the forward verging thrusts should have a listric or "sledrunner" geometry, since $\psi_b = \pi/4 - \phi/2$ so $\delta_b = 0$. More generally, this is true whenever there is equality in (20). In all other cases, forward

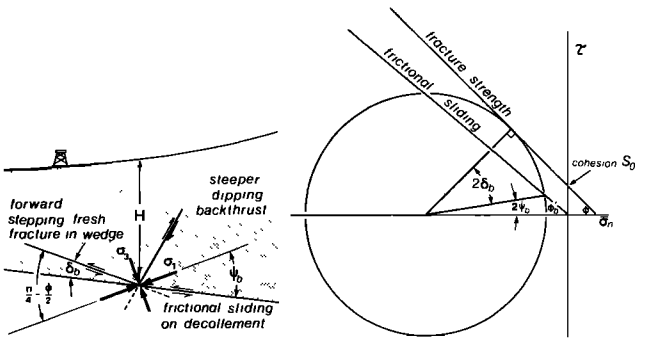

Fig. 4. Geometry of Coulomb fractures stepping up from the basal decollement and Mohr diagram illustrating the basal state of effective stress.

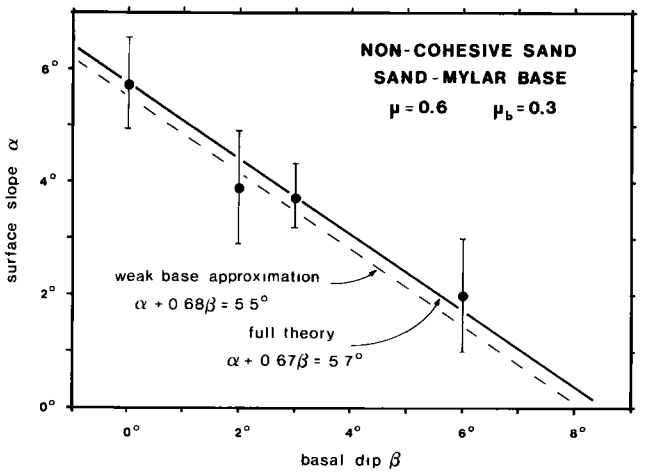

Fig. 5. Comparison of theoretical critical surface slope with measured mean slopes in sandbox experiments. Data are same as in Wedge 1 but show in addition the formal experimental error bars.

verging thrusts step up from the base at a finite angle, which should be the normal geologic situation.

The frictional traction on the basal decollement is

$$|\tau_b| = \mu_b(1 - \lambda_b)\rho g H \tag{33}$$

and the shear traction on the thrusts at the point where they step up is the fracture strength (1), which reduces to

$$|\tau| = \cos\phi \csc 2\psi_b[\mu_b(1 - \lambda_b)\rho g H] \tag{34}$$

The quantity

$$\chi = |\tau_b|/|\tau| = \sin 2\psi_b/\cos\phi \tag{35}$$

is a useful measure of the ratio of decollement strength to the overall wedge strength. In general this ratio must be in the range

$$0 \le \chi \le 1 \tag{36}$$

where the upper limit corresponds to the case of identical properties or, more generally, equality in (20).

A Weak Basal Decollement

The above results can be simplified if the decollement is very weak compared with the wedge strength so that $\chi \ll 1$, or equivalently,

$$\mu_b(1 - \lambda_b) \ll \mu(1 - \lambda) + S_0/\rho g H \tag{37}$$

The angle ψ_b is in that case small, i.e., $\psi_b \ll 1$, and (29) and (30) reduce to

$$\psi_b \approx \frac{1}{2}\left(\frac{1 - \sin\phi}{1 + \sin\phi}\right)^{1/2}\left[\frac{\mu_b(1 - \lambda_b)}{\mu(1 - \lambda) + S_0/\rho g H}\right] \tag{38}$$

Both the integrals K and Q can be approximated by their upper bounds

$$K \approx Q \approx \frac{2}{\csc\phi - 1} \tag{39}$$

so that

$$\alpha + \beta \approx \left[(1 - \rho_w/\rho)\beta + (1 - \lambda_b)\mu_b - \left(\frac{2}{\csc\phi - 1}\right)\left(\frac{S_0}{\rho g r}\right)\cot\phi\right] \cdot \left[(1 - \rho_w/\rho) + (1 - \lambda)\left(\frac{2}{\csc\phi - 1}\right)\right]^{-1} \tag{40}$$

In addition, the approximation (23) is valid throughout the wedge; in fact equating ψ at $\theta = \alpha + \beta$ to (38) yields (40).

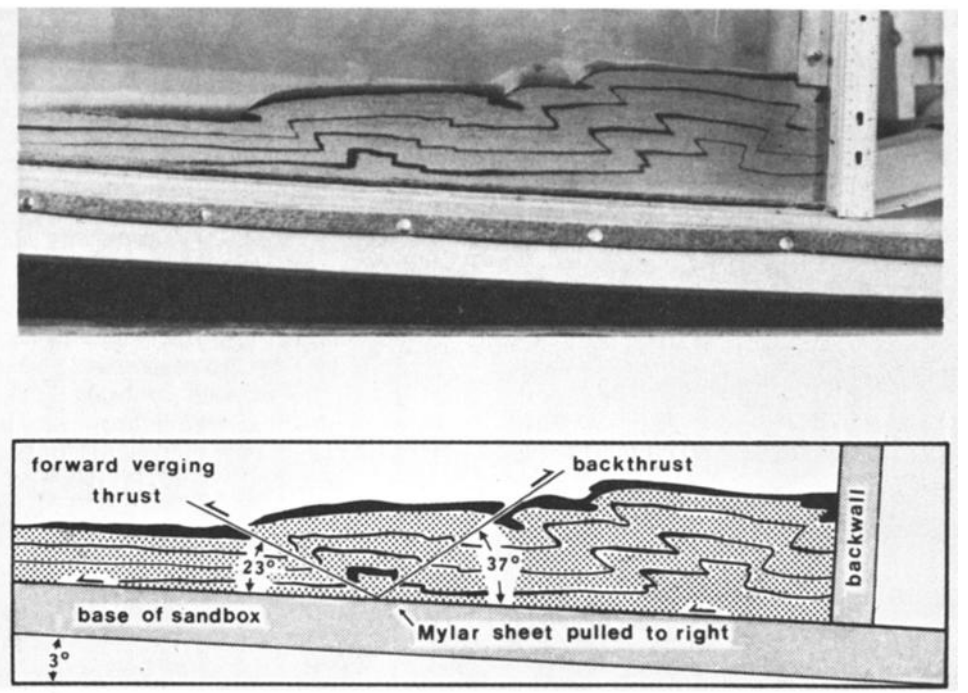

Fig. 6. Photographic side view of a deforming sand wedge, showing development of horstlike uplift bounded by pairs of forward and backward verging thrusts. The dip of each thrust generally increases after its original formation due to continued deformation. Black sand layers are passive markers.

TABLE 1. Mean and Standard Deviation of Observed Step-Up Angles in Sandbox Experiment Compared With Theoretical Angles Assuming $\mu = 0.6$ and $\mu_b = 0.3$

	Angle	Observed, deg	Exact Theory, deg	Weak-Base Approximation, deg
Forward thrusts	δ_b	22.3 ± 2.3	20.9	21.4
Back thrusts	$\delta_b + 2\psi_b$	38.5 ± 4.5	38.1	37.6

In the noncohesive case, (32) giving ψ_b is exact.

Comparing (24), (38), and (40) we see that the limiting taper far from the toe can be written most simply as

$$\alpha + \beta \approx \psi_b - \psi_0 \tag{41}$$

The slip lines or thrust faults in this weak-base noncohesive limit are straight, or planar, since $\psi \approx \psi_0 + \theta$.

Confirmation With Laboratory Sandbox Model

The parameter values appropriate to the laboratory sandbox model described in paper 1 are $S_0 = 0$, $\lambda = \lambda_b = 0$, $\mu \approx 0.6$, and $\mu_b \approx 0.3$. The critical-taper equation (17) for a dry subaerial noncohesive wedge reduces to

$$\alpha + \beta = \frac{\beta + \mu_b}{1 + K} \tag{42}$$

The integral K in this case is very nearly constant over the range of experiments, $0° \le \beta \le 6°$. With $\mu = 0.6$ and $\mu_b = 0.3$, the value obtained by numerical quadrature is $K = 2.02$; the analytical weak-base approximation (39) gives $K \approx 2.12$. These two predictions are compared with the experimental observations in Figure 5. The agreement of both is well within the experimental uncertainty, and the weak-base approximation is in this case adequate.

By stratifying the sand with passive black marker beds, the nature of the deformation within the wedge can be observed clearly during an experimental run. In general, the deformation is dominated by motion along a few discrete forward and backward verging thrust faults (see Figure 6). Faults form initially near the rigid buttress at the back of the wedge, and the locus of active faulting moves toward the toe as deformation progresses. The basal step-up angles of 23 forward thrusts and 15 back thrusts were measured off photographs. Only freshly formed faults undistorted by subsequent faulting or rotation were included in the observations. The measurements are compared with the theoretically predicted step-up angles in Table 1. Once again, the agreement with the theory is excellent. The evident success of the critical wedge theory on the laboratory scale encourages its application to more complicated and less well constrained geological situations.

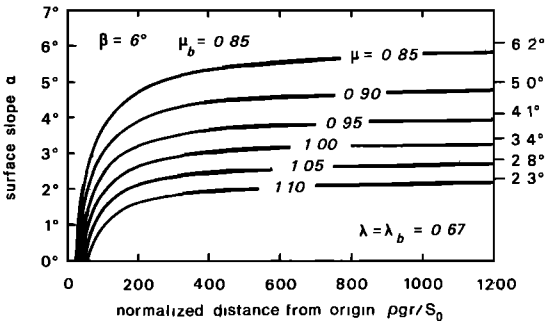

Fig. 7. Critical surface slope versus normalized distance from origin $\rho gr/S_0$. Parameters are appropriate to Taiwan.

Application of Theory to Taiwan

An introduction to the tectonic setting of the active fold-and-thrust belt of western Taiwan, including a demonstration that the wedge is presently at critical taper, is given in Wedge 1. The parameter values characterizing Taiwan are also discussed in detail there, and are summarized in Table 2. In all modeling reported here we have adopted a regional decollement dip $\beta = 6°$, fluid-pressure ratio $\lambda = \lambda_b = 0.67$, and rock density $\rho = 2500$ kg/m^3. Extensive drilling data, supplemented by seismic reflection profiling, provide the basis for these estimates; wells in the foothills that intersect the basal decolle-

TABLE 2. Measured and Inferred Parameters of Western Taiwan Fold-and-Thrust Belt

Parameter	Value	Method of Determination With Reference
Overall surface slope α, deg	2.9 ± 0.3	Linear regression of topographic profiles [*Davis et al.* 1983]; more detailed fitting in this paper
Regional decollement dip β, deg	6 ± 1	Seismic reflection profiling and deep drilling; best constrained in front 30 km of wedge [*Davis et al.*, 1983]
Density ρ, kg/m^3	2400–2700	Direct measurement of core samples and sonic logs in wells [*Namson*, 1982; this paper]
Fluid-pressure ratio λ	0.67 ± 0.05	Formation pressure tests and sonic logs in wells; at least in the foothill zone $\lambda = \lambda_b$ [*Suppe and Wittke*, 1977; *Davis et al.*, 1983]
Thrust step-up angle δ_b, deg	13.3 ± 2.4	Surface mapping, downhole dip-meter surveys and seismic profiling; inferred from theory of fault-bend folding [*Suppe*, 1983; *Namson*, 1982; this paper]
Basal coefficient of friction μ_b	0.85	Assumed; based on laboratory measurements of maximum friction of many silicate rock types [*Byerlee*, 1978]
Internal coefficient of friction μ	0.9–1.0	Inferred using critical Coulomb wedge theory (this paper)
Wedge cohesion S_0, MPa	5–20	Inferred using critical Coulomb wedge theory (this paper)
Strength ratio χ	0.4–0.5	Inferred (this paper)

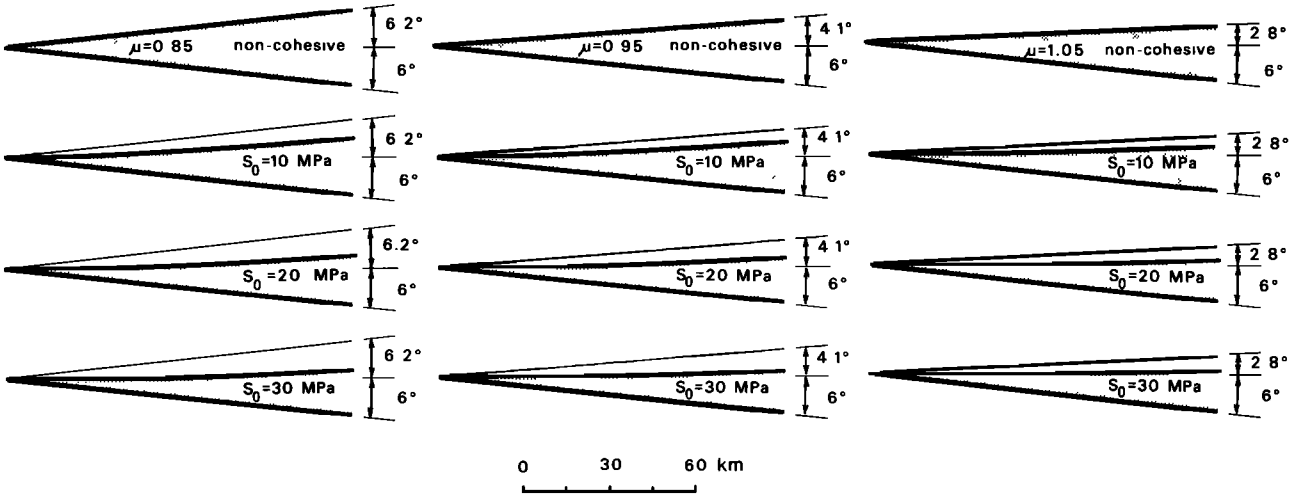

Fig. 8. Suite of theoretical critical wedge profiles having $\rho = 2500$ kg/m^3, $\lambda = \lambda_b = 0.67$, and $\mu_b = 0.85$.

ment confirm that $\lambda = \lambda_b$. The value of ρ is also that measured in the foothills, which is where we have reliable step-up angle data. In the Central Mountains, where deeper rocks are now exposed, the mean density is closer to 2700 kg/m^3; we have ignored this density increase in our modeling. To begin with, we assume that Byerlee's law $\mu_b = 0.85$ is applicable on the base, although later we explore the consequences of relaxing that assumption. The remaining two unknown strength parameters are the internal coefficient of friction μ and the wedge cohesion S_0, which we now infer from the observed surface topography and the step-up angles of thrust faults near the deformation front. Guided by our noncohesive results in Wedge 1, we do not employ the weak-base approximation in what follows.

Fitting the Surface Topography

The critical-taper equation (17) for a subaerial fold-and-thrust belt with $\lambda = \lambda_b$ reduces to

$$\alpha + \beta = \frac{\beta + (1 - \lambda)\mu_b - Q(S_0/\rho g r)\cot\phi}{1 + (1 - \lambda)K} \tag{43}$$

The decrease in surface slope toward the toe of a cohesive wedge is illustrated for Taiwan conditions in Figure 7, which

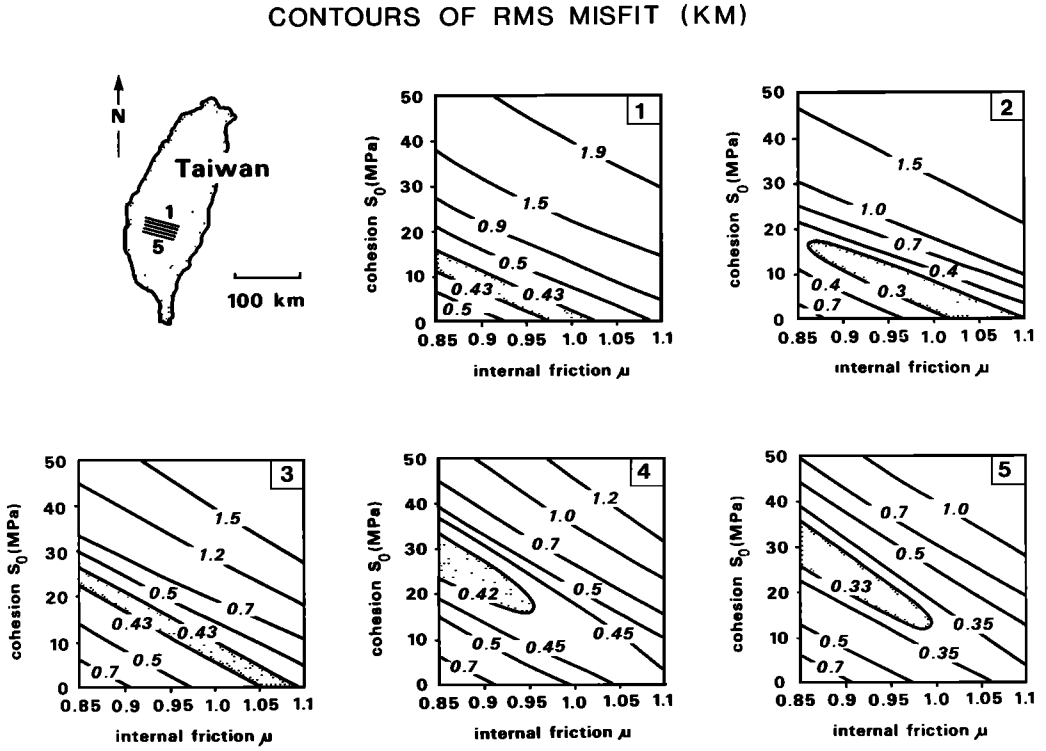

Fig. 9. Contours of root-mean-square misfit for profiles 1–5, located as shown on sketch map. Shaded regions denote set of wedge strength parameters providing best fit to observed topography.

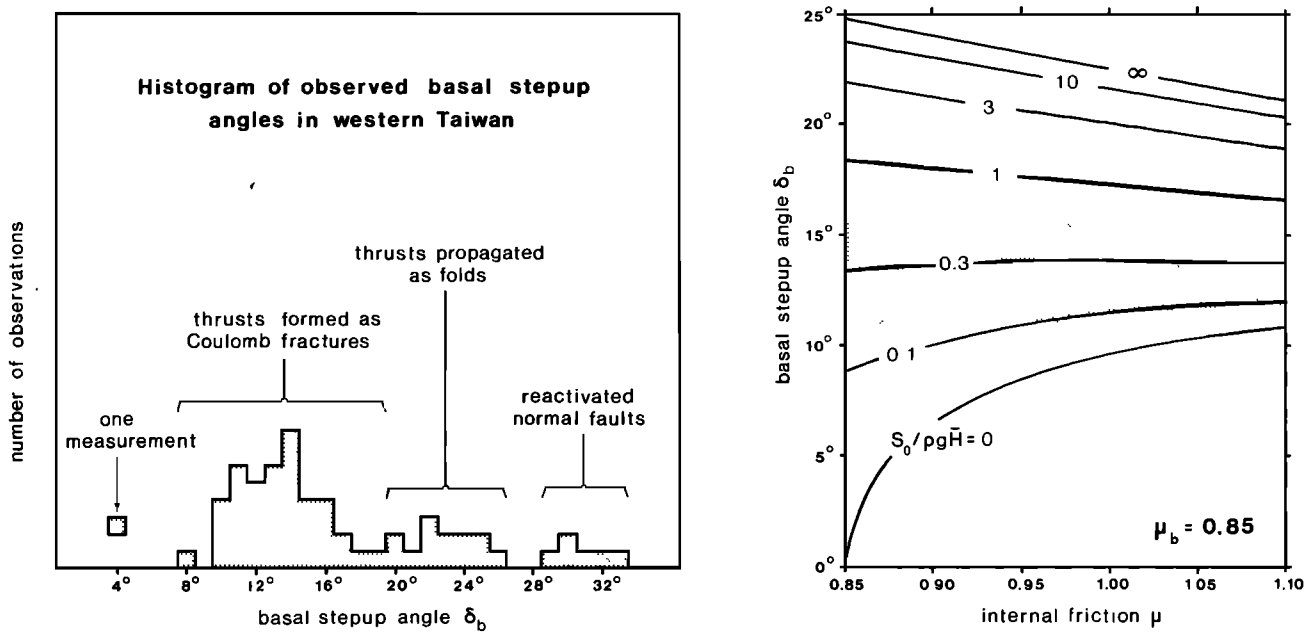

Fig. 10. Observed step-up angles of thrust faults near toe of wedge in western Taiwan compared with theoretical step-up angle for various values of wedge strength parameters.

is a plot of α versus $\rho g r/S_0$ for various values of μ in the range $0.85 \leq \mu \leq 1.10$. The noncohesive asymptotes corresponding to $\rho g r/S_0 \rightarrow \infty$ are given on the right. Note in passing that the normalized lengths of the undeformed Hubbert-Rubey toe are in the range $\rho g r_0/S_0 = 27$–55, which justifies the approximation (12). The curvature $d\alpha/dr$ is most pronounced near $r = r_0$, decreasing monotonically as r increases and the surface slope asymptotically approaches its noncohesive value. In Wedge 1 we inferred a coefficient of internal friction $\mu = 1.03$ from the average overall surface slope $\alpha = 2.9° \pm 0.3°$, ignor-

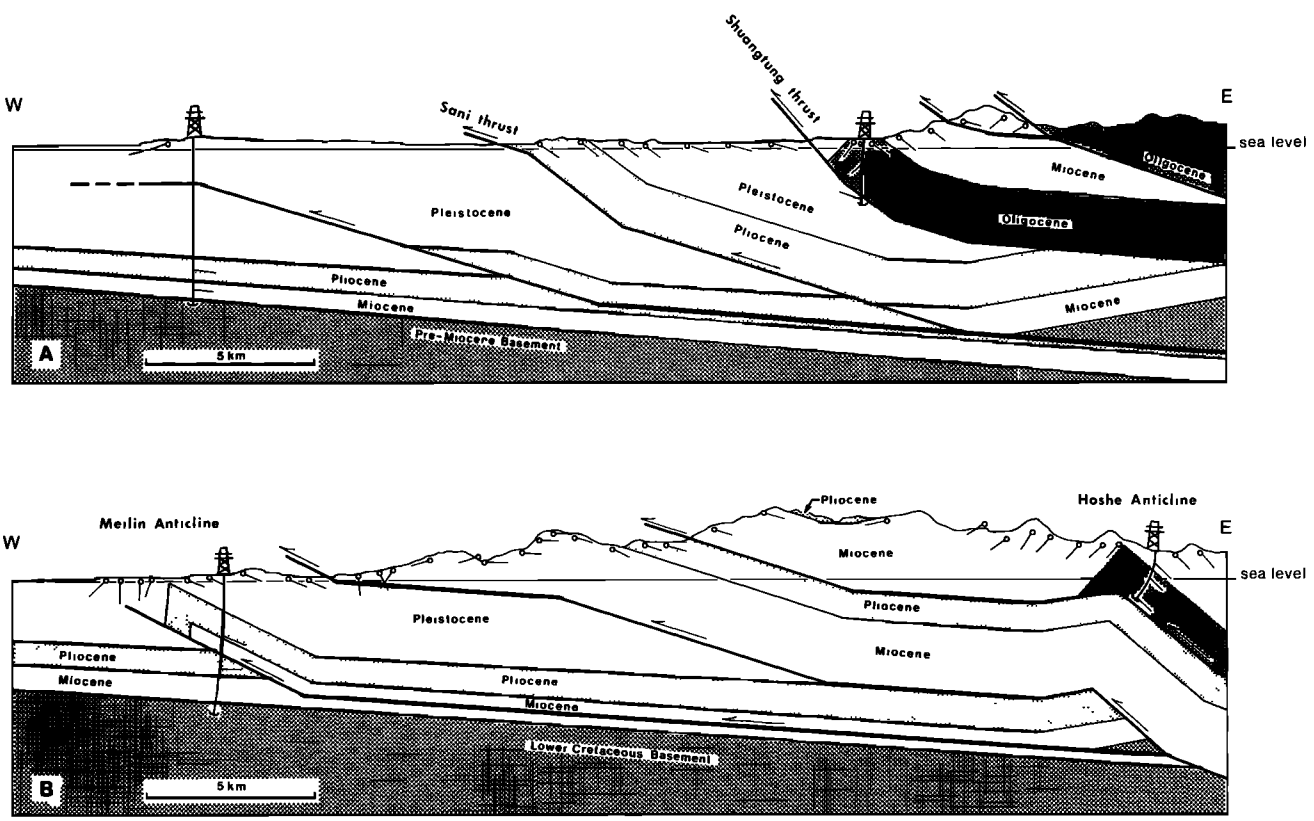

Fig. 11. Cross sections near toe of Taiwan wedge in vicinity of profiles 1–5, showing nature of step-up angle observations.

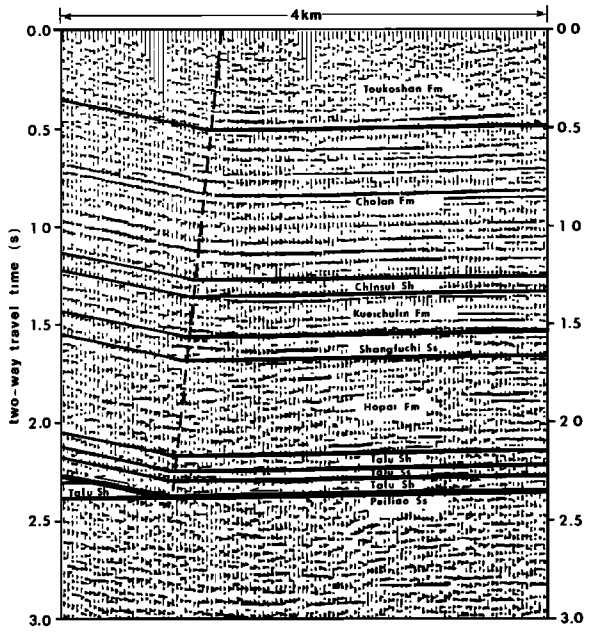

Fig. 12. Seismic time section near toe of wedge in northwestern Taiwan with structural interpretation by *Namson* [1982] showing fault-bend fold produced by thrust fault stepping up from decollement at base of Talu Shale. Data courtesy of Chinese Petroleum Corporation. Scale is approximately 1 : 1.

ing cohesion. For wedges of finite length r and cohesion S_0 we must consider the shape of the topographic profiles in more detail.

To illustrate the dependence of the critical wedge shape on the parameters μ and S_0, we have plotted a suite of cross sections, all for $\mu_b = 0.85$, in Figure 8. An increase in either μ or S_0 corresponds to a strengthening of the wedge material, leading to a decrease in the overall taper, since a stronger wedge can be thinner and still not undergo internal deformation while being thrust over a basal decollement. It is clear from the theoretical profiles that the concave curvature produced by a geologically reasonable cohesion is a subtle, essentially second-order, effect for typical wedge lengths of order 100 km. To first order, the three wedges corresponding to $\mu = 0.85$ with $S_0 = 20$ MPa, $\mu = 0.95$ with $S_0 = 10$ MPa, and $\mu = 1.05$ with $S_0 = 0$ all have very similar shapes, which might be difficult to discriminate in the presence of any small-scale topographic irregularities. This expectation has been confirmed by the results of the detailed topographic fitting we now describe.

Five profiles in the active region of deformation in central western Taiwan were selected for fitting. The profiles are oriented perpendicular to the mountain belt and extend from the deformation front at the edge of the coastal plain in the west to the highest part of the Central Mountains of Taiwan in the east; the spacing between profiles is 10 km. The depth to the basal decollement is variable across the region of fitting, going from $H = 3.5$ km just east of the deformation front on the northernmost profile to $H = 7.5$ km at a similar position on the southernmost profile. More detailed information about the topography of western Taiwan may be found in *Suppe* [1981]; the profiles we have labeled 1–5 are numbers 170–130 in his compilation.

In Figure 9 we show contours of the misfit for the five profiles, for various values of μ and S_0, assuming $\mu_b = 0.85$. For each trial value of μ and S_0, we have allowed the vertex of the theoretical wedge to move along the basal decollement until obtaining a best fit, and the contoured misfit is the rms residual of this least-squares best fit. As anticipated, there is a tradeoff between μ and S_0 that cannot be resolved by topographic fitting alone. The five profiles can be fit equally well by choosing $\mu = \mu_b = 0.85$ with S_0 in the range 15–30 MPa or by choosing μ in the range 1.0–1.1 with negligible cohesion; the latter possibility agrees, as expected, with that deduced earlier in Wedge 1. The magnitude of the misfit is approximately 300–450 m, which is the amplitude of the valley and ridge topography in western Taiwan.

Step-Up Angle of Thrusts

We can better constrain the wedge strength parameters μ and S_0 in Taiwan by taking account of the angles at which thrust faults step up from the basal decollement. In Figure 10 we show a histogram of observed step-up angles of forward verging thrusts near the toe of the wedge in the western foothills. Data are from well-constrained fault and decollement dips based on surface mapping, coring and downhole dip meter surveys, and seismic reflection profiling [*Suppe and Namson*, 1979; *Namson*, 1982; *Suppe*, 1983, and unpublished data]. Figures 11 and 12 illustrate the nature of the data. Thrusts that reach the surface have dips defined by the dip of the beds in the hanging wall, such as the Sani thrust in Figure 11*a*. Some faults are further constrained by drilling, such as the Shuangtung thrust farther to the east in the same cross section. Many faults are folded as a result of deeper imbrications, including both the Sani and Shuangtung thrusts. The basal step-up angle data shown in the histogram have been corrected for any later folding of this sort, using the methods of *Suppe* [1983].

Three peaks are apparent in the histogram: a major peak at $\delta_b = 10°–17°$ and minor ones at $\delta_b = 20°–25°$ and $\delta_b = 30°–35°$. The steepest dipping faults are known or suspected to be reactivated normal faults; an example is shown at depth under the Hoshe anticline in Figure 11*b*. The faults dipping at 20°–25° are known or suspected to propagate by the process of fault-propagation folding [*Suppe*, 1985] in which a fold grows concurrently ahead of the propagating fault tip. The Meilin anticline near the toe in Figure 11*b* is an example of this structural phenomenon. Upon eliminating probable reactivated normal faults and data thought to be complicated by fault-propagation folding, we are left with 42 faults that we believe to be relatively clean Coulomb fractures stepping up into the wedge. Both the Sani thrust and its neighbor to the west fall into this category; the fault stepping up from the base of the Talu Shale in Figure 12 is another example.

The mean and standard deviation of the step-up angles of the 42 presumed Coulomb fractures is

$$\delta_b = 13.3° \pm 2.4° \tag{44}$$

which is shown as the shaded band on the right of Figure 10.

We now consider the implications of this observation for the wedge rock properties. Equation (29) defining ψ_b reduces in the case $\lambda = \lambda_b$ to

$$\mu\mu_b \cos 2\psi_b + (\mu + S_0/\rho g\bar{H}) \sin 2\psi_b = \mu_b(1 + \mu^2)^{1/2} \tag{45}$$

in terms of the effective depth $\bar{H}$; we can likewise simplify (30) by setting $\phi_b' = \phi_b$. Theoretical values of δ_b for $\mu_b = 0.85$ and various values of μ and $S_0/\rho g\bar{H}$ are shown on the right of Figure 10, superimposed on the observed band of step-up angles. It is seen that the observations require the dimension-

less cohesion to be in the range $S_0/\rho g\bar{H} = 0.2$–0.35, essentially independent of μ over the range considered. The thickness near the toe is $H = 3.5$–7.5 km, which implies $S_0 = 5$–20 MPa. Zero cohesion is definitely precluded by the observed suite of step-up angles, as long as $\mu_b = 0.85$.

If $S_0 = 5$–20 MPa, we see from the tradeoff plots (Figure 9) that the coefficient of internal friction must be somewhere in the range $\mu = 0.9$–1.0. The best-fitting theoretical wedge profiles, assuming $\mu = 0.95$, are compared with the actual topography for the five studied sections in Figure 13. Also shown for each of the five sections is the location of the deformation front, where folding and thrusting first begins, and the position where the depth to the decollement is best determined. Undeformed foredeep and coastal plain sediments, which have not yet been accreted, lie to the west of the deformation front, where they cover the unfitted theoretical critical profiles. The values of S_0 yielding the best fits are in the range 5–20 MPA, as expected.

The variation of ψ with angular depth θ at various points in the wedge is illustrated in Figure 14 for the case $\mu = 0.95$. Just in back of the Hubbert-Rubey toe, where $\alpha = 0°$, it can be seen that $\psi \approx \theta$ to a very good approximation; this corresponds to a state of stress in which $\bar{\sigma}_1$ is horizontal at all depths. As the distance from the origin r and the slope α increase, so does ψ until in the limit $r \to \infty$ the basal inclination $\psi_b \to 14.8°$. The development of a cohesion-dominated upper boundary layer near the back of the wedge is apparent; the absolute thickness of the cohesion-dominated region is constant, but its thickness relative to that of the wedge as a whole decreases away from the toe. For surface slopes in the range $\alpha = 2°$–$3°$, as observed in western Taiwan, cohesion is important throughout the wedge, and the dip relative to horizontal $\psi - \theta$ of $\bar{\sigma}_1$ is at most a few degrees. This implies that fault inclinations that are unaffected by subsequent folding should show little variation with depth in the wedge and only moderate variation with distance from the toe.

The ratio χ of decollement strength to wedge strength is shown for various values of μ and $S_0/\rho g\bar{H}$ in Figure 15. For the values just found, namely, $\mu = 0.9$–1.0 and $S_0/\rho g\bar{H} = 0.2$–0.35, the ratio is seen to be $\chi = 0.4$–0.5.

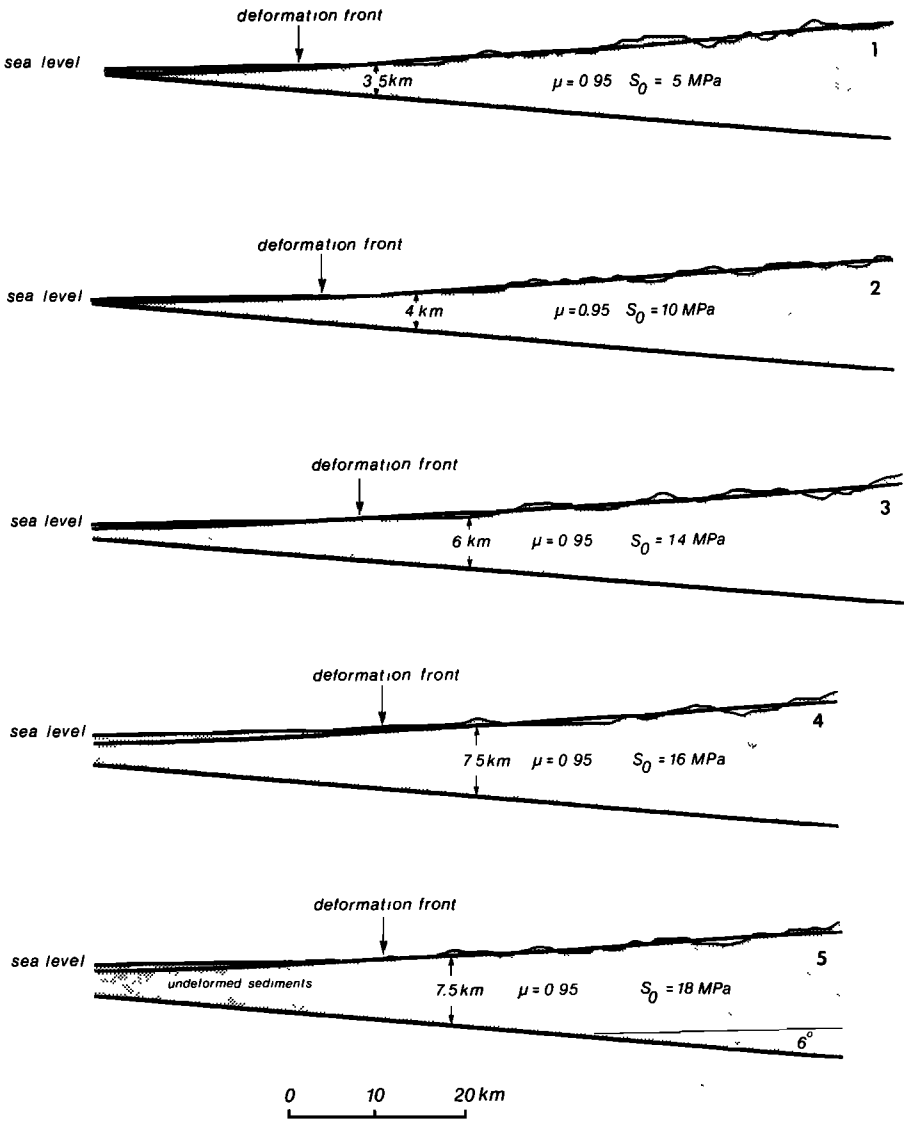

Fig. 13. Best-fitting theoretical cohesive critical wedges compared with observed topography along profiles 1–5. Coefficient of internal friction has been fixed at $\mu = 0.95$.

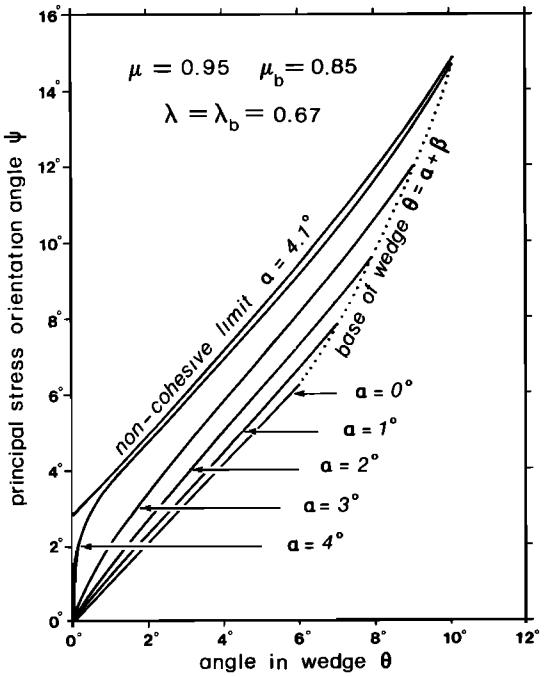

Fig. 14. Inclination ψ of $\bar{\sigma}_1$ with respect to local radius vector as a function of angular depth at several locations in wedge, assuming $\beta = 6°$. Normalized distances from origin corresponding to $\alpha = 0°$–$4°$ are $\rho g r/S_0 = 34, 47, 75, 154$, and 1725, respectively.

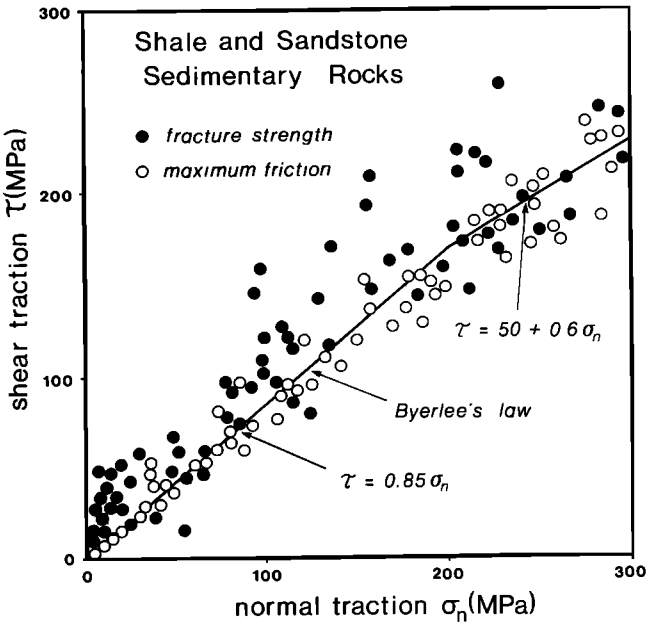

Fig. 16. Summary of laboratory measurements of fracture strength and maximum friction of dry shales and sandstones. Data from *Hoshino et al.* [1972] and *Byerlee* [1978].

DISCUSSION OF RESULTS

The wedge strength parameters inferred above are in excellent agreement with laboratory measurements of the fracture strength of sedimentary rocks. For example, Figure 16 shows the fracture strengths measured by *Hoshino et al.* [1972] on Tertiary shales and sandstones, i.e., rocks very similar to those of the Taiwan fold-and-thrust belt. Some typical maximum friction data for shales and sandstones from *Byerlee* [1978] are shown for comparison, together with his empirical fit summarizing the results of many other measurements. The fresh fracture data are, as expected, more scattered than the friction data, but it is clear that for $|\sigma_n| \leq 200$ MPa they can be adequately characterized by a cohesion in the range $S_0 = 5$–20 MPa and a coefficient of internal friction μ slightly greater than 0.85. An independent study of faults at an outcrop scale of 1–10 m in Pleistocene sediments of eastern Taiwan also suggests that $\mu \gtrsim 0.85$, based on the angle $(90° - \phi)$ between conjugate fault sets [*Barrier et al.*, 1982]. This good agreement between the macroscopic wedge parameters and laboratory fracture data suggests that the strength is controlled principally by the need to fracture locked geological structures in order for continued deformation to occur.

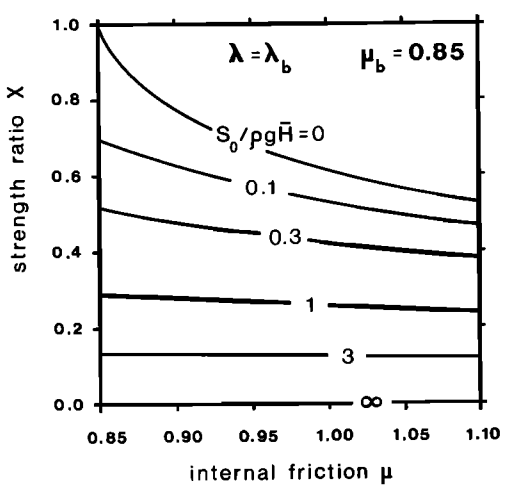

Fig. 15. Ratio χ of basal strength to wedge strength for various values of internal friction and cohesion.

Another aspect of the deformation must be the occurrence of frictional sliding along already established faults that were either formed earlier as fractures in the wedge or that may have existed previously. In either case the fault surfaces may become folded owing to deeper imbrications, leading to a wide range of fault orientations within the wedge. The theoretical range of fault orientations that can accommodate frictional sliding can be easily determined from the Mohr circle geometry shown in Figure 17. The limiting dips with respect to the local radius vector for forward verging faults are given by

$$\delta_{\max,\min} = \delta + \tfrac{1}{2}(\phi - \phi_b') \pm \tfrac{1}{2}\gamma \tag{46}$$

where δ is the corresponding dip of fresh fractures, given by (27), and

$$\cos\gamma = \frac{\sin\phi_b'[1 + (S_0/\rho g\bar{H})\cos\phi\cos 2\psi]}{\sin\phi + (S_0/\rho g\bar{H})\cos\phi} \tag{47}$$

The quantities δ, $\delta_{\max}$, and $\delta_{\min}$ have been plotted as a function of θ for Taiwan fluid-pressure conditions at two locations, where the surface slope is, respectively, $\alpha = 2°$ and $\alpha = 3°$, in Figure 18. It can be seen that faults with dips as steep as $\delta_{\max} = 35°$ can exhibit frictional sliding throughout a large part of the active Taiwan wedge. This is consistent, at least qualitatively, with both the observed imbricate steepening of Coulomb fractures and the reactivation of preexisting normal faults as discussed above.

As a final comparison, we show in Figure 19 a theoretical

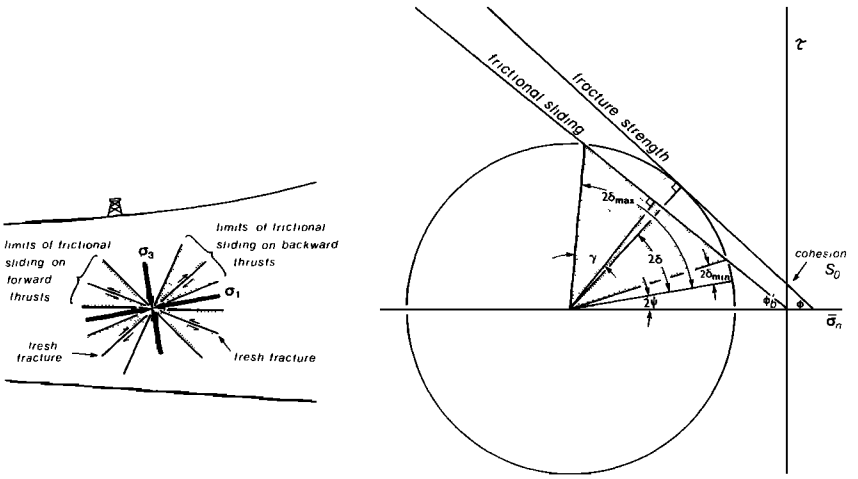

Fig. 17. Schematic depiction of preexisting fault orientations on which frictional sliding can occur. Dip of forward verging faults relative to local radius vector must be in range $\delta_{min} < \delta < \delta_{max}$, denoted by shaded triangle in Mohr diagram.

critical wedge cross section with slip lines calculated using $\mu_b = 0.85$, $\mu = 0.95$, and $S_0 = 12$ MPa together with a simplified geological cross section drawn to the same scale. Three features deserve comment. The first is that the geologic section from Taiwan is dominated by large slip on a few faults in contrast with the continuous state of failure within the theoretical wedge. This observation of widely spaced faults need not imply a significant conflict between theory and observation. For example, the bulk of the deformation of the sandbox wedge, which is known to obey the theory, was along discrete major faults. Furthermore, field observations in Taiwan indicate that the rock is cut by numerous minor faults with spacings of tens of meters and slips of decimeters to meters, suggesting that the wedge is at or near failure throughout. The second feature to note is that the region of undeformed sediments lying to the west of the deformation front is 2–3 times as extensive as the theoretical undeformed Hubbert-Rubey toe. The constant influx of sediments eroded off the growing wedge to the east essentially keeps the critical taper buried, thus inhibiting deformation. The third feature is the predominance of forward thrusting over back thrusting; at present only 2–3 back thrusts, all with poorly constrained step-up angles, are known in western Taiwan. This predominance is typical of other fold-and-thrust belts as well and must be attributed to factors that have been neglected in the above analysis. One such factor is the finite nature of the deformation. Freshly fractured forward thrusts can accommodate a greater amount of horizontal shortening for a given increase in gravitational potential energy than the more steeply dipping freshly fractured backthrusts, and this should tend to favor them, particularly if the shortening is extensive. Another factor that may be important is anisotropy; forward thrusts are more likely to coincide intermittently with stratigraphically controlled planes of weakness because their shallower dip is closer to bedding. Essentially equal amounts of forward thrusting and back thrusting are observed in the lab-

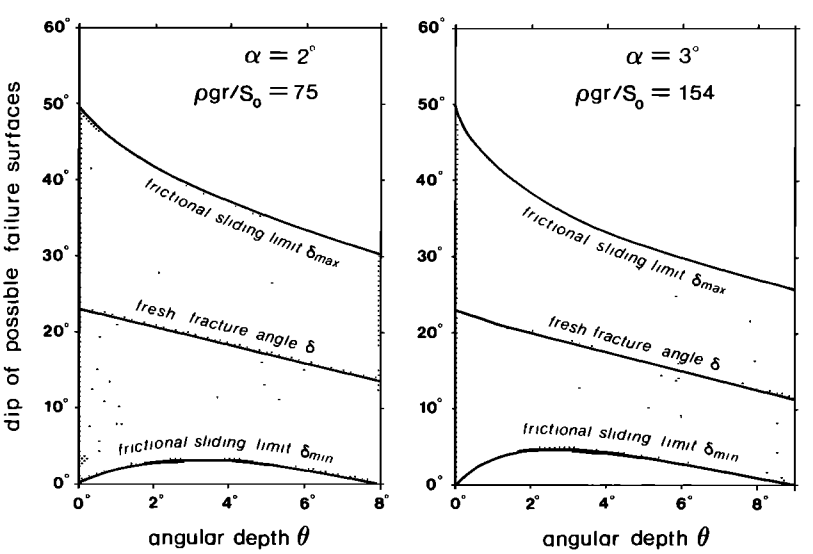

Fig. 18. Frictional sliding limits, specified as dip with respect to local radius vector, at two locations in wedge for Taiwan conditions $\beta = 6°$, $\lambda = \lambda_b = 0.67$, $\mu_b = 0.85$, and $\mu = 0.95$. Corresponding dip relative to horizontal is $\delta - \theta + \alpha$.

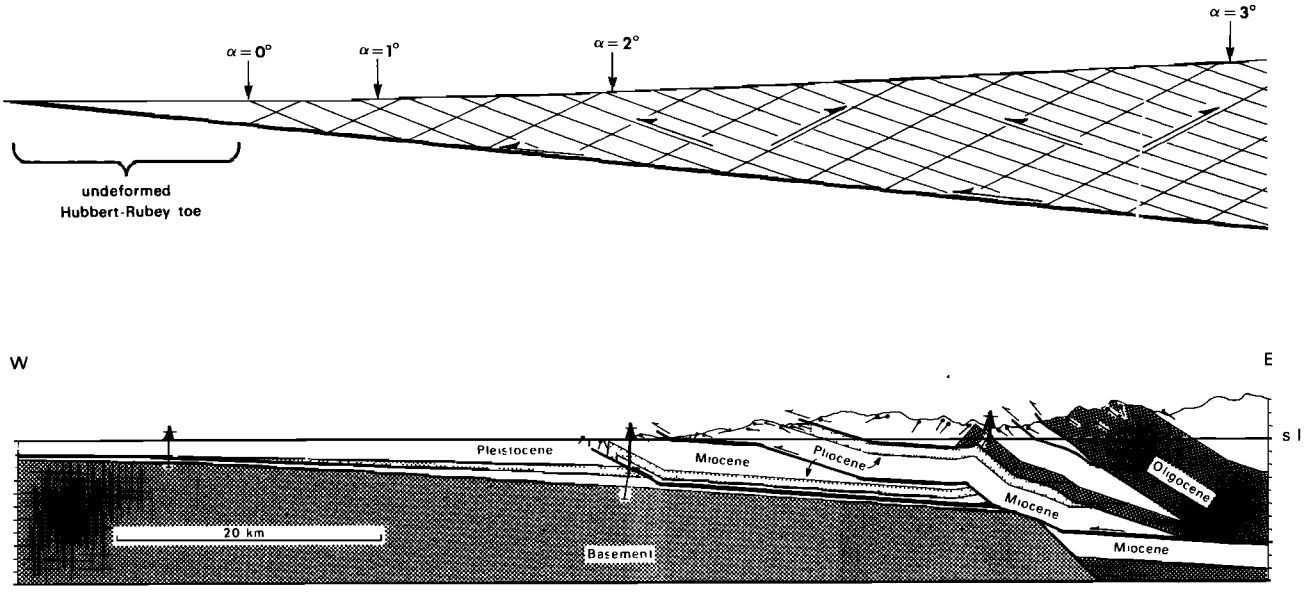

Fig. 19. Theoretical cohesive Coulomb wedge cross section with slip lines superimposed, calculated using inferred Taiwan parameters, compared with simplified geological cross section in vicinity of profiles 1–5. See Figure 11*b* for details.

oratory sandbox experiment, where anisotropy is presumably not present and the total shortening is not too great. Finally, it should be noted that back thrusts of small displacement in Taiwan or any other mountain belt would be difficult to observe geologically.

Dependence on Basal Friction Coefficient

The above results are all predicated on our use of Byerlee's law $\mu_b = 0.85$ to describe the friction on the base. The principal argument favoring the use of this law is its widespread applicability in describing the results of laboratory measurements for a variety of silicate rock types. Some a posteriori support for the choice may be drawn from the close correspondence between the inferred wedge strength parameters and laboratory fracture strength measurements, but this cannot be said to justify it completely. There is still considerable skepticism about whether laboratory studies of relatively pristine small samples are truly representative of the strength of complex rock bodies in situ, on the much larger scales of geological interest. Apart from this question of a possible dependence of rock strength on scale and structural complexity, it is known that a few materials, notably clays and clay-rich fault gouges, exhibit laboratory frictional coefficients substantially lower than Byerlee's law, in the range 0.3–0.6 [*Morrow et al.*, 1982]. Because of these questions, we now consider briefly the effect of other choices of the basal friction coefficient μ_b in Taiwan.

The results are summarized in Figure 20, which shows the locus of values μ and μ_b consistent with the overall surface slope $\alpha = 2.9°$ in the absence of cohesion, and those consistent with the step-up angle $\delta_b = 13.3°$ for various indicated values of S_0. Any cohesive wedge capable of fitting the observed taper must lie between the noncohesive locus shown and the existence limit $\mu = \mu_b$. The range of values of μ and μ_b consistent with both the taper and step-up angle is indicated, roughly, by the stippled band. It is seen that regional rock strengths considerably lower than typical laboratory values cannot be eliminated solely on the basis of the field-scale observations in Taiwan. In particular, the near coincidence of the two noncohesive loci in the interval $\mu_b \approx 0.2$–0.6 defines a family of low-strength solutions having $S_0 \approx 0$ and μ about 20% greater than μ_b. If $\mu_b = 0.85$, the shear traction on the basal decollement at a representative depth $H = 10$ km is $|\tau_b| = 65$ MPa; the lowest traction allowed by the data is on the other hand $|\tau_b| \approx 15$ MPa if $\mu_b \approx 0.2$. One final point to be noted is that the two conclusions $\mu_b \gtrsim 0.6$ and $S_0 = 5$–20 MPa are mutually dependent, since not only does the former imply the latter but vice versa.

Conclusions

A self-consistent theory for the mechanics of thin-skinned accretionary Coulomb wedges has been developed and applied to the active fold-and-thrust belt of western Taiwan. Five wedge strength parameters, in addition to the decollement dip β and wedge density ρ, characterize the state of stress in a critically tapered wedge: the internal and basal fluid-pressure ratios λ and λ_b, the internal and basal coefficients of friction μ and μ_b, and the wedge cohesion S_0. In Taiwan, $\beta = 6°$, $\rho = 2500$ kg/m^3, and $\lambda = \lambda_b = 0.67$ are measured quantities, and the remaining three parameters are constrained by two observations, namely, the overall taper of the mountain belt and the basal step-up angle of forward verging thrust faults near the toe. A model utilizing Byerlee's law $\mu_b = 0.85$ on the base and having $\mu = 0.9$–1.0 and $S_0 = 5$–20 MPa in the wedge is in good agreement with these observations as well as with laboratory fracture strength data for shales and sandstones. On this basis we conclude that continued deformation of the Taiwan fold-and-thrust belt is resisted principally by the presence of locked geological structures requiring fracture. The wedge is definitely not so pervasively fractured that frictional sliding governed by Byerlee's law is possible everywhere within it on surfaces of optimum orientation. If it were, so that $\mu = \mu_b = 0.85$ and $S_0 = 0$, it would have an overall surface slope roughly twice as steep and listric thrust faults stepping up from its base. Other solutions having proportionally lower

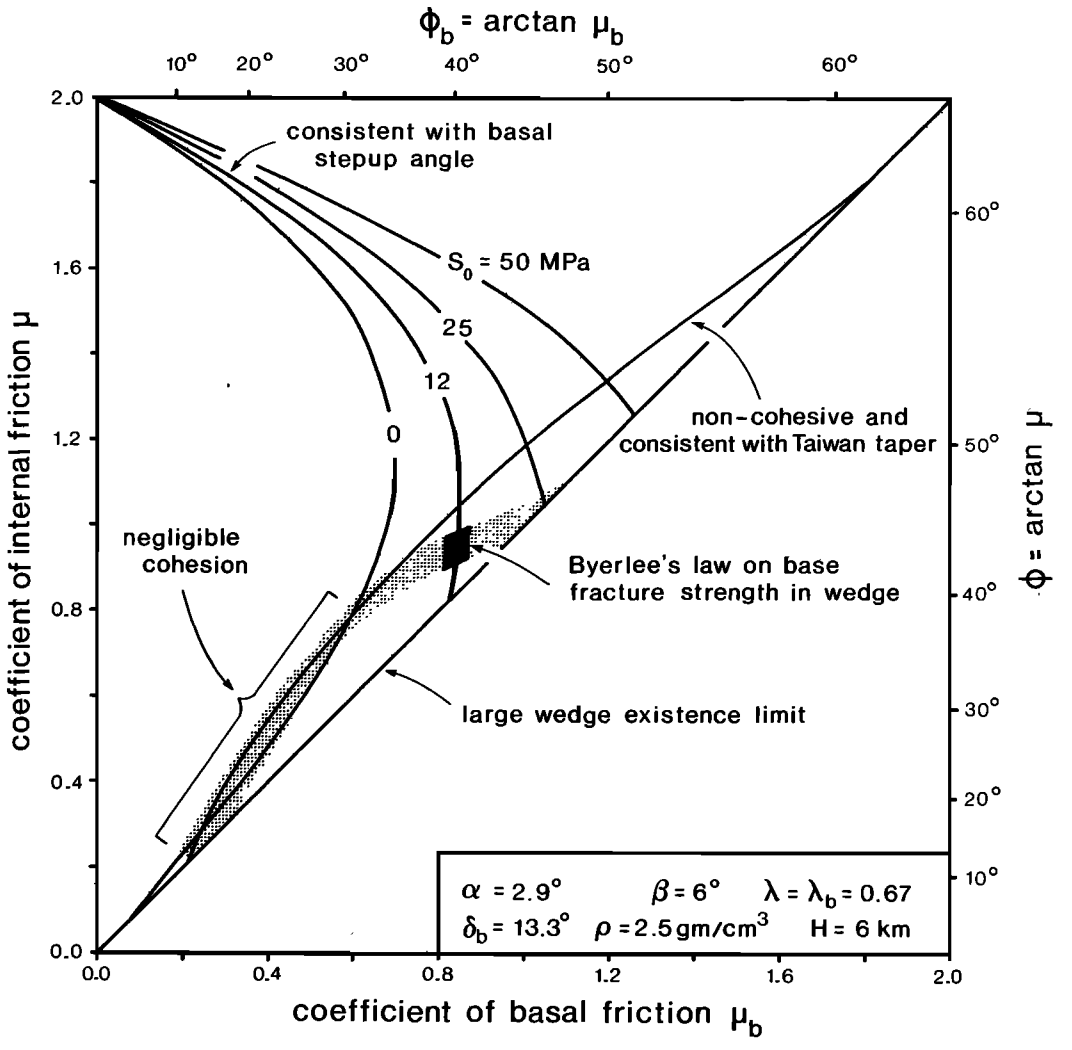

Fig. 20. Locus of possible wedge and basal strength conditions consistent with both average Taiwan taper and basal step-up angle. Models consistent with laboratory rock strengths occupy solid region.

strengths, as low as $\mu_b \approx 0.2$ and $S_0 \approx 0$, are also compatible with the Taiwan data. What is best constrained is that the parameter $\mu + S_0/\rho g\bar{H}$, where $\bar{H} = (1 - \lambda)H$ is the effective wedge thickness, must be about 20% greater than μ_b.

Acknowledgments. It is with profound sadness, fond memories, and lasting respect that we dedicate this paper to Tom Crough. While at Princeton, he was instrumental in interesting F.A.D. in quantitative tectonic modeling problems like that addressed here. We also gratefully acknowledge discussions with Glen Stockmal and the assistance of Janet Laane and Jay Namson. This work was supported by the Earth Sciences Division of the National Science Foundation under grants EAR81-21196 and EA81-21197 at Princeton and EAR78-12936 at MIT, and by the National Aeronautics and Space Administration under contract NAS5-27339 at MIT.

REFERENCES

Barrier, E., J. Angelier, H. T. Chu, and L. S. Teng, Tectonic analysis of compressional structure in an active collisional zone: The deformation of the Pinanshan conglomerates, eastern Taiwan, *Proc. Geol. Soc. China, 25*, 123–138, 1982.

Byerlee, J., Friction of rocks, *Pure Appl. Geophys., 116*, 615–626, 1978.

Chapple, W. M., Mechanics of thin-skinned fold-and-thrust belts, *Geol. Soc. Am. Bull., 89*, 1189–1198, 1978.

Davis, D., J. Suppe, and F. A. Dahlen, Mechanics of fold-and-thrust belts and accretionary wedges, *J. Geophys. Res., 88*, 1153–1172, 1983.

Hill, R., *The Mathematical Theory of Plasticity*, 355 pp., Clarendon, Oxford, 1950.

Hoshino, K., H. Koide, K. Inami, S. Iwamura, and S. Mitsui, Mechanical properties of Japanese Tertiary sedimentary rocks under high confining pressures, *Rep. 244*, 200 pp., Geol. Surv. of Japan, Kawasaki, 1972.

Hubbert, M. K., and W. W. Rubey, Role of fluid pressure in mechanics of overthrust faulting, 1, Mechanics of fluid-filled solids and its application to overthrust faulting, *Geol. Soc. Am. Bull., 70*, 115–166, 1959.

Jaeger, J. C., and N. G. W. Cook, *Fundamentals of Rock Mechanics*, pp. 87–91, Methuen, London, 1969.

Morrow, C. A., L. Q. Shi, and J. D. Byerlee, Strain hardening and strength of clay-rich fault gouges, *J. Geophys. Res., 87*, 6771–6780, 1982.

Namson, J. S., Studies of the structure, stratigraphic record of plate interaction and role of pore-fluid pressure in the active fold and thrust belt of Taiwan and a study of manganese deposits from northern California, Ph.D. thesis, 302 pp., Princeton Univ., Princeton, N. J., 1982.

Stockmal, G. S., Modeling of large-scale accretionary wedge formation, *J. Geophys. Res., 88*, 8271–8287, 1983.

Suppe, J., Mechanics of mountain building and metamorphism in Taiwan, *Geol. Soc. China Mem., 4*, 67–89, 1981.

Suppe, J., Geometry and kinematics of fault-bend folding, *Am. J. Sci.*, *283*, 684–721, 1983.

Suppe, J., *Principles of Structural Geometry*, pp. 348–352, Prentice-Hall, Englewood Cliffs, N. J., 1985.

Suppe, J., and J. Namson, Fault-bend origin of frontal folds of the western Taiwan fold-and-thrust belt, *Petrol. Geol. Taiwan*, *16*, 1–18, 1979.

Suppe, J., and J. H. Wittke, Abnormal pore-fluid pressures in relation to stratigraphy and structure in the active fold-and-thrust belt of northwestern Taiwan, *Petrol. Geol. Taiwan*, *14*, 11–24, 1977.

F. A. Dahlen and J. Suppe, Department of Geological and Geophysical Sciences, Guyot Hall, Princeton University, Princeton, NJ 08544.

D. Davis, Lamont-Doherty Geological Observatory of Columbia University, Palisades, NY 10964.

(Received August 29, 1983;
revised February 17, 1984;
accepted March 9, 1984.)